Organic & Biomolecular Chemistry

ROYAL SOCIETY OF CHEMISTRY

PAPER

View Article Online
View Journal | View Issue

Cite this: *Org. Biomol. Chem.*, 2022, **20**, 1299

Hydrofluorocarbon nanoparticles for ^{19}F MRI-fluorescence dual imaging and chemo-photodynamic therapy†

Tingjuan Wu,‡[a,b] Kexin Chen,‡[a,b] Mou Jiang,[c] Anfeng Li,[a] Xingxing Peng,[a] Shizhen Chen,[c] Zhigang Yang,[b] Xin Zhou,[c] Xing Zheng*[a] and Zhong-Xing Jiang*[b,c]

The synergistic chemotherapy and photodynamic therapy (PDT) may significantly improve the cancer therapeutic efficacy, in which fluorinated nanoemulsions are highly advantageous for their ability to deliver oxygen to hypoxic tumors and provide fluorine-19 magnetic resonance imaging (^{19}F MRI). The low solubility of chemotherapy drugs and photosensitizers in current perfluorocarbon (PFC)-based ^{19}F MRI agents usually leads to complicated formulations or chemical modifications and low nanoemulsion stability and performance. Herein, we employ readily available partially fluorinated ethyl 2-(3,5-bis(trifluoromethyl)phenyl)acetate as the ^{19}F MRI agent and the solvent to dissolve the cancer stem cell inhibitor salinomycin and the photosensitizer ICG for the convenient preparation of ^{19}F MRI-fluorescence dual imaging and synergistic chemotherapy, photothermal and photodynamic therapy nanoemulsions. The chemotherapy drug salinomycin has a high solubility in the partially fluorinated reagent, facilitating its high loading and efficient delivery. Paramagnetic iron(III) (Fe^{3+}) is incorporated into the nanoemulsion through the dissolved chelator to significantly improve the ^{19}F MRI sensitivity. Furthermore, the dissolved fluorinated 2-pyridone enables the efficient capture and sustained release of singlet oxygen in the dark for high PDT efficacy. The multifunctional nanoemulsions show sensitive ^{19}F MRI and fluorescence dual imaging capability and high synergistic chemotherapy, photothermal and photodynamic therapy efficacy in cancer cells, which may be valuable oxygen delivery, sustained ROS generating and release, dual imaging and multimodal therapy agents for hypoxic tumors. This study provided a convenient co-solubilization strategy for the rapid construction of multifunctional theranostics for hypoxic tumors.

Received 8th December 2021,
Accepted 18th January 2022

DOI: 10.1039/d1ob02392f

rsc.li/obc

Introduction

Since its invention in 1977,[1] ^{19}F MRI has attracted considerable attention in biomedicine because of its ability to generate high contrast "hot-spot" images without background interference, ionizing radiation, and tissue depth limit.[2] In recent years, ^{19}F MRI has been increasingly incorporated into multimodal imaging systems and theranostics to assist disease diagnosis and drug therapy, such as ^{19}F MRI-guided drug therapy,[3] *in vivo* ^{19}F MRI cell tracking,[4] *etc.* ^{19}F MRI agents play a crucial role in these systems as ^{19}F signal sources and interact with other functions, in which the integration of ^{19}F MRI and other functions is of great importance for the successful application of these systems. Besides fluorinated polymers and complicated synthetic molecules,[5] PFC nanoemulsions are the overwhelmingly used ^{19}F MRI agents.[1–4] However, the high fluorine contents and heavy fluorous properties[6] of PFCs lead to many issues of PFC-based ^{19}F MRI agents, such as complicated formulations, severe organ retention, and challenges in

[a]*Group of Lead Compound, Department of Pharmacy, Hunan Provincial Key Laboratory of Tumor Microenvironment Responsive Drug Research, Hunan Province Cooperative Innovation Center for Molecular Target New Drug Study, University of South China, Hengyang 421001, China. E-mail: zhengxing9166@sohu.com*
[b]*Hubei Province Engineering and Technology Research Center for Fluorinated Pharmaceuticals, School of Pharmaceutical Sciences, Wuhan University, Wuhan 430071, China. E-mail: zxjiang@whu.edu.cn*
[c]*State Key Laboratory of Magnetic Resonance and Atomic and Molecular Physics, National Center for Magnetic Resonance in Wuhan, Wuhan Institute of Physics and Mathematics, Innovation Academy for Precision Measurement Science and Technology, Chinese Academy of Sciences – Wuhan National Laboratory for Optoelectronics, Huazhong University of Science and Technology, Wuhan, 430071, China*

†Electronic supplementary information (ESI) available: Synthesis of 2-pyridone **9**, preparation and characterization of the nanoemulsions, ^{19}F MRI phantom experiments, photothermal and photodynamic experiments, cellular uptake study, cytotoxicity assay, *in vitro* anticancer efficacy, and copies of spectra. See DOI: 10.1039/d1ob02392f

‡These authors contributed equally to this work.

functionalization and conjugation.[7] Therefore, replacing PFCs with partially fluorinated agents (hydrofluorocarbons, HFCs) may address these issues and facilitate the convenient integration of other functions by simply dissolving functional agents instead of complicated chemical modification.

Among the ^{19}F MRI-containing multifunctional theranostics, ^{19}F MRI-fluorescence dual imaging and synergistic chemo- and photodynamic cancer therapy systems are desirable. In terms of imaging, ^{19}F MRI and fluorescence imaging perfectly complement each other, which facilitates the high-resolution and sensitive fluorescence imaging for *in vivo* studies and highly selective and tissue-depth-limit-free ^{19}F MRI for *in vitro* studies.[8] In terms of therapy, the ^{19}F MRI agents can track the theranostics, help relieve the tumor hypoxia, and even provide information of tumor microenvironments. Tumor hypoxia is a common issue that hampers the radio-, chemo-, and photodynamic therapy of cancer.[9] In cancer PDT, the hypoxic tumor microenvironment would significantly reduce ROS generation due to the lack of local oxygen. It is noteworthy that fluorocarbons are well known for their high oxygen dissolving capability, which has been employed to deliver oxygen to the hypoxic tumor.[10] Meanwhile, fluorocarbons are valuable oxygen probes, the so-called ^{19}F NMR/MRI oximetry,[11] which provide the concentration and distribution of local oxygen in the tumor through the oxygen-sensitive ^{19}F longitudinal relaxation time T_1. With the ability to dissolve, deliver and monitor oxygen, ^{19}F MRI-containing PDT theranostics may relieve tumor hypoxia and optimize the PDT for high therapeutic efficacy.

Herein, we employed readily available HFCs as ^{19}F MRI agents and solvents to dissolve the chemotherapy drugs, photosensitizers, and tumor hypoxia relieving agents for the convenient preparation of ^{19}F MRI-fluorescence dual imaging chemotherapy-PDT nanoemulsions, aiming to address the issues associated with PFC-based nanoemulsions (Fig. 1). Commercially available methyl 3,5-bis(trifluoromethyl) benzoate **1** and ethyl 2-(3,5-bis(trifluoromethyl)phenyl)acetate **2** were selected as the HFCs. The six symmetrical fluorines in esters **1** and **2** provide a unified ^{19}F NMR signal for sensitive ^{19}F MRI. At the same time, their relatively low fluorine contents (F%: **1** 42%, **2** 38%) may avoid the issues of PFCs (F%: >60%) and improve the co-solubility of functional agents, including chelator **3**, stable free radical TEMPO **4**, chemotherapy drugs (salinomycin **5**, paclitaxel **6**, camptothecin **7**, and atovaquone **8**), 2-pyridone **9**, and photosensitizer **10**. Chelator **3** can improve the ^{19}F MRI sensitivity through the paramagnetic relaxation enhancement (PRE) effect of chelated Fe^{3+}. Besides the dissolving and delivering of oxygen by fluorocarbons **1**–**3**, 2-pyridone **9** may capture singlet oxygen during laser irradiation and release it in the dark for sustained PDT,[12] while the oxidative phosphorylation inhibitor atovaquone **8** may reduce the local oxygen consumption for high PDT efficacy.[13] ICG **10** was employed as the fluorescent dye and photothermal and photodynamic agent. Besides providing fluorescence imaging, PDT and photothermal therapy (PTT), ICG may also control the release of chemotherapy drugs, hypoxia relieving agents and ROS dissolved in the nanoemulsions by elevating the local temperature.

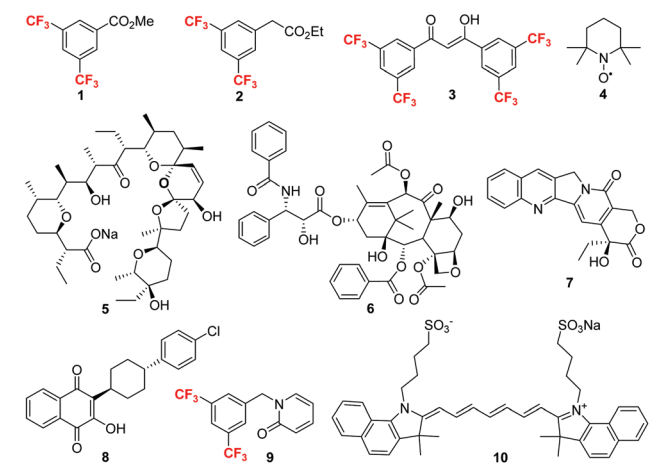

Fig. 1 Chemical structures of compounds **1**–**10**.

Results and discussion

Partially fluorinated esters **1** and **2** are commercially available liquid chemicals at room temperature, ideal for formulating nanoemulsions. In order to simplify the synthesis and provide a ^{19}F signal close to ester **2**, fluorinated 2-pyridone **9** was designed and conveniently synthesized from 3,5-bis(trifluoromethyl) benzyl bromide in one step on a gram scale (see the ESI†). The solubilities of functional agents **3**–**10** in esters **1** and **2** were then investigated at weight percentages of 1%, 5%, and 20%. Because of the same 3,5-bis(trifluoromethyl)phenyl moiety, chelator **3** and 2-pyridone **9** showed considerable solubility in esters **1** and **2** (Fig. 2a and b, weight percentages for **3**

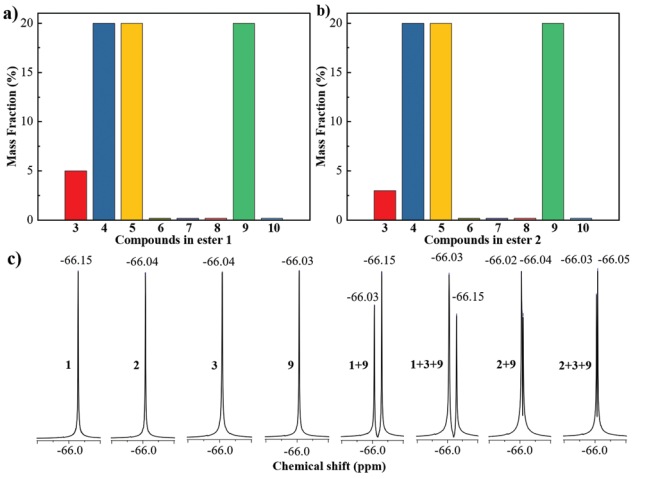

Fig. 2 The co-solubilities of agents **3**–**10** in esters **1** (a) and **2** (b) at weight percentages of 1%, 5% and 20%, and partial ^{19}F NMR (376 MHz, $CDCl_3$ as the solvent) spectra of reagents **1**–**3** and **9** and their mixtures of equal weights as indicated (c).

in **1**: 5%, **9** in **1**: >20%, **3** in **2**: 3%, **9** in **2**: >20%). Stable free radical TEMPO **4** showed high solubility of over 20% in both esters, and the resulting mixtures may be potential dynamic nuclear polarization (DNP) agents for supersensitive hyperpolarized ^{19}F MRI.[14] Among the chemotherapy drugs, salinomycin **5** had good solubilities of over 20% in both esters, while paclitaxel **6**, camptothecin **7** and atovaquone **8** had very poor solubilities of less than 1% in both esters, respectively. The photosensitizer ICG **10** also showed poor solubility in both esters. These results suggested that esters **1** and **2** prefer to dissolve non-aromatic and non-charged compounds with a low aggregation tendency. As for comparison, compounds **3**, **5–10** showed negligible solubility in perfluorooctyl bromide (PFOB, a typical PFC in ^{19}F MRI), while TEMPO **4** showed over 20% solubility in PFOB. As expected, fluorinated compounds **1–3** and **9** gave an intense singlet ^{19}F NMR peak around 66.0 ppm from their all chemically equivalent fluorines, respectively (Fig. 2c). As expected, the mixture of ester **2** and 2-pyridone **9** gave very close ^{19}F NMR peaks ($\Delta\delta$ = 0.02 ppm). Moreover, the mixture of ester **2**, chelator **3** and 2-pyridone **9** still gave very close ^{19}F NMR peaks, which would be highly preferred for improving the ^{19}F MRI sensitivity by generating images from all the fluorines in the nanoemulsions (Fig. 2c). In comparison, the mixtures of ester **1**, chelator **3** and 2-pyridone **9** gave two distant ^{19}F NMR peaks. Interestingly, the signal of chelator **3** coincided with either ester **1** or 2-pyridone **9** in the mixtures.

Because of their good co-solubility, ester **2**, chelator **3**, salinomycin **5** and 2-pyridone **9** were chosen to formulate the multifunctional nanoemulsions. Notably, ester **2** instead of ester **1** was chosen as the leading ^{19}F MRI signal source and the solvent because ester **2** has a lower fluorine content and a very close ^{19}F NMR peak to chelator **3** and 2-pyridone **9**. After many initial screenings of the formulations, the combination of surfactants S75, F68 and soybean oil provided monodisperse nanoemulsion **E2** of ester **2** with a diameter of 151.6 nm and a low polydispersity index (PDI) of 0.096, in which soybean oil significantly improved the nanoemulsion stability and PDI (Table 1). Chelator **3**, salinomycin **5**, 2-pyridone **9** and ICG **10** were sequentially added into the formulations, and the corresponding nanoemulsions **E3–E7** were obtained with high monodispersity and appropriate particle sizes. After adding ferric chloride to the nanoemulsion solutions, Fe^{3+} was extracted into the nanoemulsion particles by chelator **3** and provided paramagnetic nanoemulsions **E5** and **E8**, respectively. Lipid conjugated cyclic peptide DSPE-PEG$_{2000}$-RGDyC was introduced into nanoemulsion **E9** to target integrin overexpressed cancer cells. The good co-solubility of functional agents **3**, **5**, **9** and ester **2** significantly improved the loading capability of functional agents, simplified the formulation process and provided homogeneous and monodisperse nanoemulsions.

The particle size and PDI of the nanoemulsions were measured by dynamic light scattering (DLS, Table 1). DLS shows the highly monodisperse nanoemulsions **E7** and **E8** (average diameters: **E7** 154 nm and **E8** 156 nm; PDI: **E7** 0.087 and **E8** 0.080, Fig. 3a and b). The monodispersity and spherical shape of **E7** and **E8** were further confirmed by transmission electron microscopy (TEM). The high nanoemulsion stabilities of **E7** and **E8** were detected by DLS over 15 days with negligible particle size and PDI changes.

The ^{19}F NMR properties of nanoemulsions **E7–E9** were then investigated. As designed, these nanoemulsions gave an intense unified singlet ^{19}F NMR peak at around −64.0 ppm, respectively (Fig. 4a). Nanoemulsion **E7** had a short longitudinal relaxation time T_1 of 618 ms and a transverse relaxation time T_2 of 235 ms (Fig. 4b). Compared to PFC nanoemulsions,[15] the significantly shorter relaxation times of **E7** may result from slower molecular tumbling of ester **2**, chelator **3** and 2-pyridone **9** induced by the π–π interactions of their phenyl groups. The π–π interactions were confirmed by the ^{19}F chemical shift change from −66.0 ppm of the $CDCl_3$ solution of **2**, **3** and **9** to −64.0 ppm of **2**, **3** and **9** in nanoemulsions **E7–E9** (Fig. 2c and 4a). The integration of Fe^{3+} by the dissolved chelator **3** dramatically shortens the T_1 and T_2 of nanoemulsions **E8** and **E9** by around 90% (**E8**: T_1 = 74 ms, T_2 = 21 ms; **E9**: T_1 = 78 ms, T_2 = 11 ms), respectively, which would significantly improve the ^{19}F MRI sensitivities by reducing the data collection time.[16]

The ^{19}F MRI and fluorescence imaging abilities of nanoemulsions **E7** and **E8** were also studied. The T_1-weighted ^{19}F MRI phantom images showed a significantly higher ^{19}F MRI sensitivity of **E8** than **E7**, especially at high concentrations

Table 1 Formulation ingredients, particle size, and PDI of nanoemulsions **E1–E9**

Number	Formulation ingredients[a]	Size[b] (PDI)
E1	Soybean oil, S75, F68	116 (0.129)
E2	**2**, soybean oil, S75, F68	152 (0.096)
E3	**2**, **9**, soybean oil, S75, F68	151 (0.125)
E4	**2**, **9**, **10**, soybean oil, S75, F68	121 (0.177)
E5[c]	**2**, **3**, **9**, **10**, soybean oil, S75, F68, Fe^{3+}	158 (0.136)
E6	**2**, **5**, **9**, **10**, soybean oil, S75, F68	160 (0.163)
E7	**2**, **3**, **5**, **9**, **10**, soybean oil, S75, F68	154 (0.087)
E8[c]	**2**, **3**, **5**, **9**, **10**, soybean oil, S75, F68, Fe^{3+}	156 (0.080)
E9[c]	**2**, **3**, **5**, **9**, **10**, soybean oil, S75, F68, Fe^{3+}, RGD[d]	137 (0.110)

[a] Amount of ingredients in 2 mL water: 60 mg **2**, 10 mg **9**, 1 mg **3**, 2 mg **5**, 1 mg **10**, 50 mg soybean oil, 20 mg S75, and 20 mg F68. [b] Size is the diameter in nm. [c] Fe^{3+} : chelator **3** = 1 : 4. [d] RGD represents DSPE-PEG$_{2000}$-RGDyC.

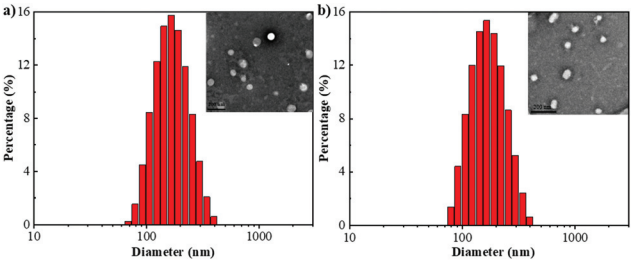

Fig. 3 DLS and TEM images of **E7** (a) and **E8** (b). The scale bar of TEM images is 200 nm.

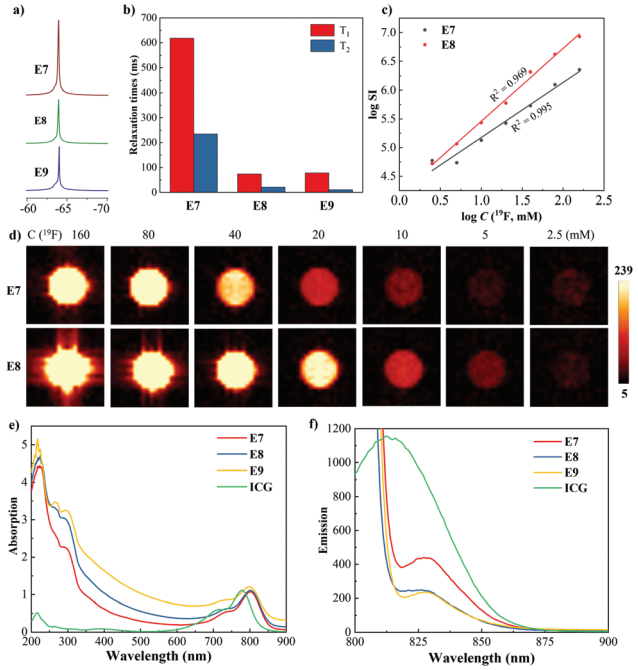

Fig. 4 Partial ^{19}F NMR spectra (a, 564 MHz) and ^{19}F relaxation times (b, 470 MHz) of **E7–E9**, T_1-weighted ^{19}F MRI phantom images (d, ^{19}F concentration as indicated) and plot of log SI *versus* log $C(^{19}F)$ (c) of **E7** and **E8**, and UV absorption spectra (e) and FL emission spectra (f) of ICG, **E7–E9** at 5 μg mL^{-1} of ICG. C(^{19}F) was calculated from the formulation of nanoemulsions.

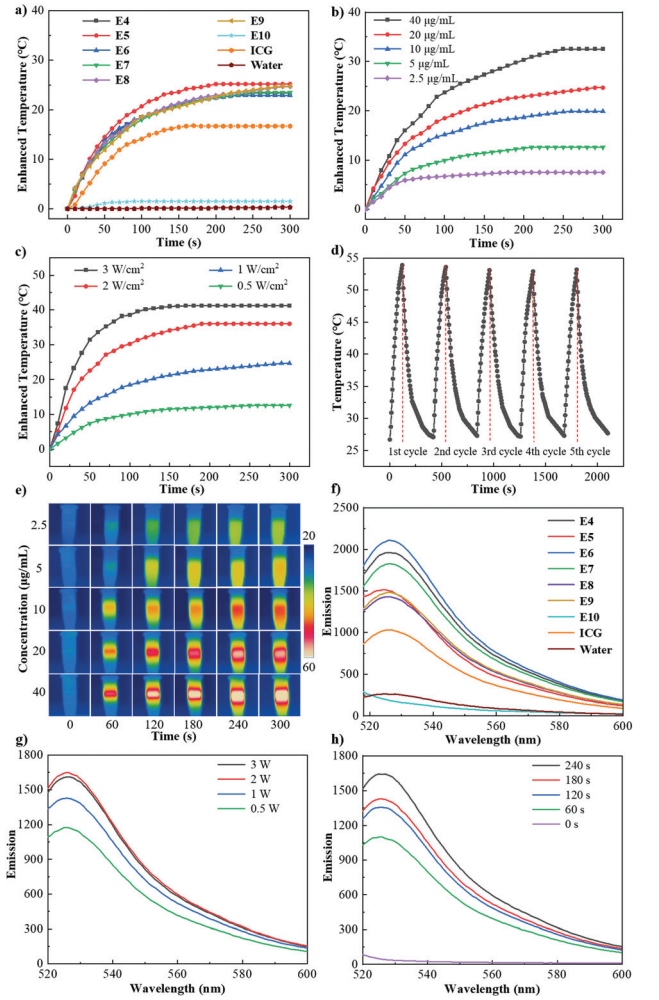

Fig. 5 Temperature elevations of laser irradiated **E4–E10** with ICG and water as controls (a, 1 W cm^{-2}, 20 μg mL^{-1}, **E10** represents **E8** without ICG), **E8** at the indicated concentrations (b, 1 W cm^{-2}), **E8** under the indicated laser power densities (c, 20 μg mL^{-1}), **E8** over five heating–cooling cycles (d, 1 W cm^{-2} irradiation for 2 min, cooling from 5 min, 40 μg mL^{-1}), thermal images of **E8** at the indicated irradiation time and concentration monitored using a thermal camera (e), the fluorescence of **E4–E10** mixed with 2.0 μM of SOSG under 1 W cm^{-2} irradiation with ICG and water as controls (f), **E8** under the indicated laser power densities (g), and **E8** under a 1 W cm^{-2} laser at the indicated irradiation times (h); unless otherwise indicated, 3 minutes of 808 nm laser irradiation and ICG of 2.5 μg mL^{-1} were used and the concentrations are referred to as ICG concentrations.

(Fig. 4d). Because the PRE effect of Fe^{3+} significantly reduced the ^{19}F T_1 by 88%, **E8** was imaged at a fluorine concentration of 2.5 mM with a data collection time of 819 seconds. The proportional relationships between the ^{19}F MRI signal intensity log SI and the logarithm of ^{19}F concentration log $C(^{19}F)$ were found in the T_1-weighted ^{19}F MRI phantom images (Fig. 4c), which facilitates the accurate quantification of the nanoemulsions with ^{19}F MRI. Compared to ICG water solution, slightly red-shifted UV absorption peaks and considerably red-shifted fluorescence emission peaks at around 825 nm were observed from the UV absorption and fluorescence emission spectra of **E7** and **E8** (Fig. 4e and f). Compared to the ICG solution, the significantly lower fluorescence intensity of **E7** and **E8** suggested the aggregation of ICG at the nanoemulsion particle surface, showing that insoluble fluorescent dyes in ^{19}F MRI agents may lead to aggregation-caused fluorescence quenching (ACQ).

Next, the therapeutic potential of the nanoemulsions was investigated. With the PTT capability of ICG, the photothermal efficacy of the nanoemulsions was first measured. Under the irradiation of an 808 nm laser at 1 W cm^{-2} for 5 minutes, dramatic temperature elevations of 23–25 °C were observed in all ICG-containing nanoemulsions **E4–E9** at an equivalent ICG concentration of 20 μg mL^{-1} (Fig. 5a). As for comparison, pure water and **E8** without ICG showed little temperature elevation while free ICG in water showed much lower temperature elevation. Concentration-dependent photothermal experiments on **E8** showed that the temperature elevation is closely related to the ICG concentration with an elevation of up to 32.5 °C at 40 μg mL^{-1} of ICG (Fig. 5b). In contrast, negligible temperature elevation of water was observed under the same conditions. Raising the laser power density from 0.5 W cm^{-2} to 3.0 W cm^{-2} led to a temperature elevation of **E8** (at 20 μg mL^{-1} of ICG) from 12.6 °C to 41.2 °C, which indicated a higher temperature elevation to kill cancer cells could be achieved by increasing the laser power density (Fig. 5c). Repetitive laser irradiation at 1 W cm^{-2} and 40 μg mL^{-1} of ICG and cooling of **E8** showed very stable temperature elevations

for at least 5 cycles (Fig. 5d). These data indicated that nanoemulsions **E4–E9** have very high and stable photothermal conversion capability for potential photothermal therapy. The photothermal conversion capability of **E8** was further visualized by the photothermal images of **E8** at a series of ICG concentrations and laser irradiation times (Fig. 5e). Notably, after the irradiation of an 808 nm laser at 1 W cm^{-2} for 5 minutes on **E8** at a high ICG concentration of 500 μg mL^{-1}, the photothermal effect caused significant structural changes from highly monodisperse nanoemulsions (diameter = 156 nm, PDI = 0.08) to a highly heterogeneous mixture (diameter = 1209 nm, PDI = 1.0), showing the rupture of nanoemulsion particles and the quite possible release of the loaded salinomycin **5** and 2-pyridone **9**.

The ROS generating ability of the nanoemulsions was measured with the fluorescent dye SOSG as a ROS probe. Under 808 nm laser irradiation at 1 W cm^{-2} for 3 minutes, high concentration ROS was generated in all the ICG-containing nanoemulsions **E4–E9** and was detected by the fluorescence of SOSG at 525 nm (Fig. 5f). Notably, **E4–E9** showed an even higher ROS generating capability than an ICG solution of the same concentration, which may be related to the nonaggregated distribution of ICG on the nanoparticle surface and the dissolved oxygen in the nanoemulsions. Compared to **E7**, Fe^{3+}-containing **E8** had lower ROS generating capability, suggesting that Fe^{3+} may partially hamper ROS generation in the systems. Increasing the laser irradiation times from 60 to 240 seconds or power densities from 0.5 to 3 W cm^{-2} on **E8** could further promote ROS generation (Fig. 5g and h).

Finally, the therapeutic potential of the nanoemulsions was investigated in cells. Compared to blank nanoemulsion **E1**, Fe^{3+} and ICG-containing **E5** showed high biocompatibilities in human breast cancer MCF-7 cells, lung cancer A549 cells and breast MCF-10A cells, which indicated low Fe^{3+}-induced toxicity and low dark toxicity of ICG at concentrations of up to 15 μg mL^{-1} (Fig. 6a–c). Compared to salinomycin, salinomycin-containing **E8** exhibited significantly higher cytotoxicity towards cancerous MCF-7 cells and A549 cells but comparable cytotoxicity towards normal breast MCF-10A cells probably due to the improved uptake of salinomycin loaded in **E8** by cancerous cells. Confocal microscopy images of A549 cells incubated with **E8** showed considerable uptake after 2 hours of incubation and high uptake after 12 hours of incubation (Fig. 6d and i). With DAPI as the nucleus dye, a high concentration of **E8** was found in the cytoplasm after 12 hours of incubation.

The PDT efficacy of nanoemulsion **E8** was investigated in A549 cells. With DCFH-DA as the green fluorescent probe for ROS, the high ROS generating ability of **E8** was observed from the intense green fluorescence in A549 cells after 12 hours of incubation with **E8** and 5 minutes of laser irradiation at 1 W cm^{-2} and an ICG concentration of 10 μg mL^{-1} (Fig. 6e and j). In contrast, no green fluorescence of DCFH-DA was observed from the control group treated with PBS and laser irradiation. The CCK-8 cytotoxicity assay was employed to evaluate the PDT efficacy of **E8** in A549 cells. Compared to salinomycin, **E8** showed dramatically higher cytotoxicity, while even higher

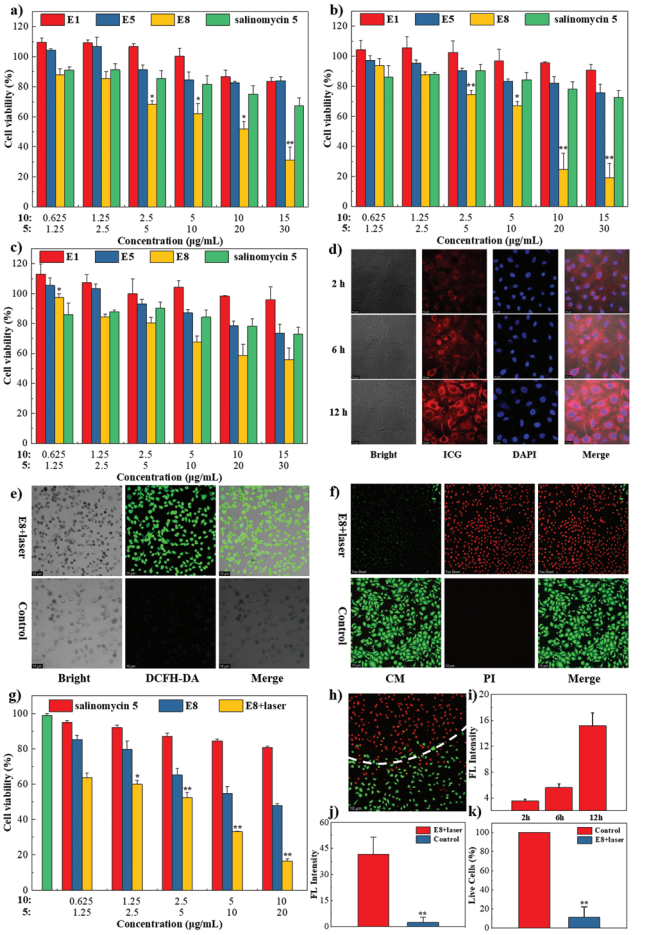

Fig. 6 CCK-8 cytotoxicity assay of nanoemulsions **E1**, **E5**, **E8** and salinomycin **5** in A549 cells (a), MCF-7 cells (b), and MCF-10A cells (c) at the indicated ICG **10** and salinomycin **5** concentrations, confocal microscopy images of A549 cells incubated with **E8** at the indicated times (d), confocal microscopy images of DCFH-DA-treated A549 cells after laser irradiation (e, upper **E8**-treated, lower PBS-treated), A549 cells after laser irradiation and calcein-AM/PI fluorescence staining (f, upper **E8**-treated, lower PBS-treated), and cytotoxicity assay of A549 cells treated with salinomycin **5**, **E8** and **E8** with laser irradiation, respectively (g), fluorescence image of live/dead cell staining on A549 cells after laser irradiation above the dashed line (h), and quantitative analysis of the fluorescence intensity in confocal microscopy images of **E8**-treated A549 cells in figure d (i), in figure e (j), and in figure f (k). The ICG **10** and salinomycin **5** concentrations were calculated from the formulation of nanoemulsions. 5 minutes of 808 nm laser irradiation at 1 W cm^{-2} was used. The values represent the means ± s.d. (n = 3 for a–d; NS, not significant; *P < 0.05, **P < 0.01 *vs.* salinomycin).

cytotoxicity was observed in the **E8**-treated A549 cells with 5 minutes of laser irradiation at 1 W cm^{-2} (Fig. 6g). The live–dead cell calcein-AM/PI fluorescence stain was used to visualize the PDT efficacy in A549 cells. With laser irradiation, slightly red fluorescence from PI-stained dead cells was observed in the PBS-treated A549 cells. After 5 minutes of laser irradiation of the **E8**-treated A549 cells at 1 W cm^{-2}, intense red fluorescence of PI-stained dead cells was found from the green fluorescence background of calcein-AM-stained live cells (Fig. 6f and k). Therefore, the high PDT efficacy of nanoemul-

sion **E8** was proved by the ROS generation in the cells, cytotoxicity assay and live–dead cell staining.

Conclusions

In summary, we have developed novel partially fluorinated nanoemulsions with ^{19}F MRI-fluorescence dual-imaging and synergistic chemotherapy, photothermal and photodynamic therapy capabilities from readily available partially fluorinated reagents, demonstrating the strategy of lowering fluorine contents and improving the co-solubility for the convenient preparation of multifunctional ^{19}F MRI nanoemulsions. Although only partially fluorinated with relatively low fluorine contents, the nanoemulsions have a unified ^{19}F peak from all fluorines and effective PRE enhancement from the dissolved Fe^{3+} for highly sensitive ^{19}F MRI. The high solubility of the chemotherapy drug salinomycin in the partially fluorinated ester facilitates its high loading, convenient delivery, and controlled release by the photothermal effect of loaded ICG. The dissolved oxygen in the fluorinated nanoemulsions and sustained release of singlet oxygen by the fluorinated 2-pyridone help to relieve the tumor hypoxia and improve the PDT efficacy, which was demonstrated in the cellular studies. This study addressed many issues of perfluorocarbon-based nanoemulsions, developed novel multifunctional ^{19}F MRI theranostics, and provided a convenient and valuable strategy to relieve tumor hypoxia. The application of these nanoemulsions in animal models is under active investigation, which will be reported in due course.

Conflicts of interest

The authors declare no competing financial interest.

Acknowledgements

We are thankful for the financial support from the National Natural Science Foundation of China (22077098 and 91859206), the National Key R&D Program of China (2018YFA0704000), Hunan Provincial Hengyang Joint Fund (2020JJ6052), and Laboratory of Tea and Health of Hengyang (202150083704).

Notes and references

1 G. N. Holland, P. A. Bottomley and W. S. Hinshaw, *J. Magn. Reson.*, 1977, **28**, 133–136.

2 For reviews, see: (*a*) J. Ruiz-Cabello, B. P. Barnett, P. A. Bottomley and J. W. M. Bulte, *NMR Biomed.*, 2011, **24**, 114–129; (*b*) I. Tirotta, V. Dichiarante, C. Pigliacelli, G. Cavallo, G. Terraneo, F. B. Bombelli, P. Metrangolo and G. Resnati, *Chem. Rev.*, 2015, **115**, 1106–1129; (*c*) L. Wu, F. Liu, S. Liu, X. Xu, Z. Liu and X. Sun, *Int. J. Nanomed.*, 2020, **15**, 7377–7395; (*d*) H. Lin, X. Tang, A. Li and J. Gao, *Adv. Mater.*, 2021, **33**, 2005657.

3 (*a*) Y. B. Yu and Z.-X. Jiang, *Drug Delivery Res.*, 2012, **1**, 1; (*b*) S. Bo, Y. Yuan, Y. Chen, Z. Yang, S. Chen, X. Zhou and Z.-X. Jiang, *Chem. Commun.*, 2018, **54**, 3875–3878.

4 (*a*) M. Srinivas, A. Heerschap, E. T. Ahrens, C. G. Figdor and I. J. M. de Vries, *Trends Biotechnol.*, 2010, **28**, 363–370; (*b*) M. Srinivas, P. Boehm-Sturm, C. G. Figdor, I. J. de Vries and M. Hoehn, *Biomaterials*, 2012, **33**, 8830–8840; (*c*) Q. Peng, Y. Li, S. Bo, Y. Yuan, Z. Yang, S. Chen, X. Zhou and Z.-X. Jiang, *Chem. Commun.*, 2018, **54**, 6000–6003.

5 (*a*) Z.-X. Jiang, X. Liu, E.-K. Jeong and Y. B. Yu, *Angew. Chem., Int. Ed.*, 2009, **48**, 4755–4758; (*b*) J. C. Knight, P. G. Edwards and S. J. Paisey, *RSC Adv.*, 2011, **1**, 1415–1425; (*c*) W. Yu, Y. Yang, S. Bo, Y. Li, S. Chen, Z. Yang, X. Zheng, Z.-X. Jiang and X. Zhou, *J. Org. Chem.*, 2015, **80**, 4443–4447; (*d*) X. Zhu, X. Tang, H. Lin, S. Shi, H. Xiong, Q. Zhou, A. Li, Q. Wang, X. Chen and J. Gao, *Chem*, 2020, **6**, 1134–1148; (*e*) X. Tang, X. Gong, A. Li, H. Lin, C. Peng, X. Zhang, X. Chen and J. Gao, *Nano Lett.*, 2020, **20**, 363–371; (*f*) T. Wu, A. Li, K. Chen, X. Peng, J. Zhang, M. Jiang, S. Chen, X. Zheng, X. Zhou and Z.-X. Jiang, *Chem. Commun.*, 2021, **57**, 7743–7757.

6 (*a*) J. A. Gladysz and D. P. Curran, *Tetrahedron*, 2002, **58**, 3823–3825; (*b*) M. Cametti, B. Crousse, P. Metrangolo, R. Milani and G. Resnati, *Chem. Soc. Rev.*, 2012, **41**, 31–42.

7 J. M. Janjic, M. Srinivas, D. K. K. Kadayakkara and E. T. Ahrens, *J. Am. Chem. Soc.*, 2008, **130**, 2832–2841.

8 (*a*) S. Mizukami, R. Takikawa, F. Sugihara, M. Shirakawa and K. Kikuchi, *Angew. Chem., Int. Ed.*, 2009, **48**, 3641–3643; (*b*) Z. Wang, X. Yue, Y. Wang, C. Qian, P. Huang, M. Lizak, G. Niu, F. Wang, P. Rong, D. O. Kiesewetter, Y. Ma and X. Chen, *Adv. Healthcare Mater.*, 2014, **3**, 1326–1333; (*c*) T. Nakamura, F. Sugihara, H. Matsushita, Y. Yoshioka, S. Mizukami and K. Kikuchi, *Chem. Sci.*, 2015, **6**, 1986–1990; (*d*) Y. Zhang, S. Bo, T. Feng, X. Qin, Y. Wan, S. Jiang, C. Li, J. Lin, T. Wang, X. Zhou, Z.-X. Jiang and P. Huang, *Adv. Mater.*, 2019, **31**, 1806444; (*e*) H. Zhang, Q. Yu, Y. Li, Z. Yang, X. Zhou, S. Chen and Z.-X. Jiang, *Chem. Commun.*, 2020, **56**, 3617–3620.

9 (*a*) J. E. Moulder and S. Rockwell, *Cancer Metastasis Rev.*, 1987, **5**, 313–341; (*b*) J. M. Brown, *Methods Enzymol.*, 2007, **435**, 295–321; (*c*) J. C. Walsh, A. Lebedev, E. Aten, K. Madsen, L. Marciano and H. C. Kolb, *Antioxid. Redox Signaling*, 2014, **21**, 1516–1554.

10 (*a*) M. Gao, C. Liang, X. Song, Q. Chen, Q. Jin, C. Wang and Z. Liu, *Adv. Mater.*, 2017, **29**, 1701429; (*b*) G. Song, C. Ji, C. Liang, X. Song, X. Yi, Z. Dong, K. Yang and Z. Liu, *Biomaterials*, 2017, **112**, 257–263; (*c*) Z. Zhou, B. Zhang, H. Wang, A. Yuan, Y. Hu and J. Wu, *Theranostics*, 2018, **8**, 4898–4911; (*d*) M. P. Krafft and J. G. Riess, *Adv. Colloid Interface Sci.*, 2021, **294**, 102407; (*e*) R. A. Day and E. M. Sletten, *Curr. Opin. Colloid Interface Sci.*, 2021, **54**, 101454.

11 (*a*) S. Hunjan, R. P. Mason, A. Constantinescu, P. Peschke, E. W. Hahn and P. P. Antich, *Int. J. Radiat. Oncol., Biol., Phys.*, 1998, **41**, 161–171; (*b*) D. K. Kadayakkara, J. M. Janjic, L. K. Pusateri, W. B. Young and E. T. Ahrens, *Magn. Reson. Med.*, 2010, **64**, 1252–1259; (*c*) A. Bol, D. Labar, B. Jordan,

J. Magat, L. Mignion, V. Grégoire and B. Gallez, *Radiother. Oncol.*, 2012, **105**, 29–35.

12 (*a*) I. S. Turan, D. Yildiz, A. Turksoy, G. Gunaydin and E. U. Akkaya, *Angew. Chem., Int. Ed.*, 2016, **55**, 2875–2878; (*b*) J. Zou, J. Zhu, Z. Yang, L. Li, W. Fan, L. He, W. Tang, L. Deng, J. Wu, Y. Ma, Y. Cheng, W. Huang, X. Dong and X. Chen, *Angew. Chem., Int. Ed.*, 2020, **59**, 8833–8838.

13 (*a*) D. Xia, P. Xu, X. Luo, J. Zhu, H. Gu, D. Huo and Y. Hu, *Adv. Funct. Mater.*, 2019, **29**, 1807294; (*b*) L. P. Zhao, R. R. Zheng, H.-Q. Chen, L. S. Liu, X.-Y. Zhao, H.-H. Liu, X.-Z. Qiu, X.-Y. Yu, H. Cheng and S.-Y. Li, *Nano Lett.*, 2020, **20**, 2062–2071.

14 (*a*) K. N. Hu, H. H. Yu, T. M. Swager and R. G. Griffin, *J. Am. Chem. Soc.*, 2004, **126**, 10844–10845; (*b*) M. Lu, M. Wang, I. V. Sergeyev, C. M. Quinn, J. Struppe, M. Rosay, W. Maas, A. M. Gronenborn and T. Polenova, *J. Am. Chem. Soc.*, 2019, **141**, 5681–5691.

15 C. Giraudeau, J. Flament, B. Marty, F. Boumezbeur, S. Mériaux, C. Robic, M. Port, N. Tsapis, E. Fattal, E. Giacomini, F. Lethimonnier, D. L. Bihan and J. Valette, *Magn. Reson. Med.*, 2010, **63**, 1119–1124.

16 A. H. Jahromi, C. Wang, S. R. Adams, W. Zhu, K. Narsinh, H. Xu, D. L. Gray, R. Y. Tsien and E. T. Ahrens, *ACS Nano*, 2018, **13**, 143–151.